A Variational r-Adaption and Shape-Optimization Method for Finite-Deformation Elasticity

P. Thoutireddy and M. Ortiz
Division of Engineering and Applied Science
California Institute of Technology
Pasadena, CA 91125

Submitted to: *International Journal for Numerical Methods in Engineering*, April 27, 2003
Corresponding author: M. Ortiz, Fax: +1-626-449-2677; e-mail: ortiz@aero.caltech.edu
Keywords: r-adaption; Variational methods; Configurational forces; Finite elements; Mesh optimization; Shape optimization.

Abstract

This paper is concerned with the formulation of a variational r-adaption method for finite-deformation elastostatic problems. The distinguishing characteristic of the method is that the variational principle simultaneously supplies the solution, the optimal mesh and, in problems of shape optimization, the equilibrium shapes of the system. This is accomplished by minimizing the energy functional with respect to the nodal field values as well as with respect to the triangulation of the domain of analysis. Energy minimization with respect to the referential nodal positions has the effect of equilibrating the energetic or *configurational forces* acting on the nodes. We derive general expressions for the configuration forces for isoparametric elements and nonlinear, possibly anisotropic, materials under general loading. We illustrate the versatility and convergence characteristics of the method by way of selected numerical tests and applications, including the problem of a semi-infinite crack in linear and nonlinear elastic bodies; and the optimization of the shape of elastic inclusions.

1 Introduction

For static problems, the displacement, conforming, finite-element method is a particular case of the Rayleigh-Ritz method, or method of constrained minimization, consisting of the minimization of a suitable energy functional over a finite-dimensional space X_h of finite-element interpolants. For elastic bodies, the appropriate energy functional to minimize is the potential energy of the body, whereas for inelastic bodies and dynamical systems appropriate energy functionals follow by recourse to time-discretization, Ortiz and Stainier [1999]; Radovitzky and Ortiz [1999].

Within this variational context, the question of mesh adaption and optimization may be understood as the determination of the *best interpolation space* X_h of a certain dimension. For linear problems, such as linear elasticity, the space of solutions has a well-defined normed-space structure, typically in the form of a Sobolev space, the solution exists and is unique under well-understood technical conditions, and standard error estimates provide bounds for the energy-norm error $|\boldsymbol{u}_h - \boldsymbol{u}|_E$, e. g., Strang and Fix [1973], provided that the solution $\boldsymbol{u}$ has sufficient regularity. A natural adaption strategy is then to optimize the mesh so that the error bound is minimized.

This approach may formally be extended to finite deformations by recourse to linearization, Radovitzky and Ortiz [1999], but in this case the coercivity of the linearized energy norm and the regularity of the

solution can no longer be guaranteed in general. Worse still, for fully nonlinear problems, including finite kinematics, the solution may not be unique due to geometrical instabilities such as buckling, or solutions may not exist outright due to material instabilities and the attendant lack of lower semi-continuity of the energy functional, Evans [1998]. Furthermore, for nonlinear problems, no natural norm may generally be defined measuring the distance between exact and approximate solutions, and the entire conceptual framework of *energy-norm errors* and *error bounds* simply collapses.

An alternative approach which applies naturally to nonlinear variational problems and generalizes the conventional energy-norm error framework for linear problems is to *rely on the variational principle to supply both the solution and the optimal mesh*. Thus, suppose for definiteness that we seek the stable equilibrium configurations of a nonlinear elastic material and that, consequently, the operative principle is the principle of minimum potential energy. Within this framework, the sole figure of merit which determines the quality of a deformation mapping $\boldsymbol{\varphi}$ is its potential energy $I[\boldsymbol{\varphi}]$. In particular, given two deformation mappings $\boldsymbol{\varphi}'$ and $\boldsymbol{\varphi}''$ with $I(\boldsymbol{\varphi}') < I(\boldsymbol{\varphi}'')$, then $\boldsymbol{\varphi}'$ is to be regarded as a *better* deformation mapping than $\boldsymbol{\varphi}''$. Since finite-element solutions $\boldsymbol{\varphi}_h$ are constrained minimizers, one has $E = I(\boldsymbol{\varphi}_h) - I_{\min} \geq 0$, where $I_{\min}$ is the infimum of $I[\boldsymbol{\varphi}]$, and E may be regarded as the natural measure of the 'badness', or 'error', of $\boldsymbol{\varphi}_h$. We note that, since the energy of the system is always well-defined, this notion of optimality applies equally well to linear and nonlinear problems. Of course, in linear problems orthogonality gives $E = |\boldsymbol{u}_h|_E^2 - |\boldsymbol{u}|_E^2 = |\boldsymbol{u}_h - \boldsymbol{u}|_E^2$, and E reduces to the conventional energy-norm error.

Clearly, the energy, and hence the quality, of the finite-element solution depends on the choice of mesh. Thus, in keeping with the principle of minimum potential energy, the *optimal mesh is that for which the least minimum energy is achieved*. This criterion suggests minimizing the energy with respect to both the nodal displacements as well as the triangulation. For instance, one may seek the Delaunay triangulation of a fixed number of nodes which minimizes the energy. A strategy for finding this optimal Delaunay mesh is to minimize the energy with respect to both the spatial and referential nodal positions, while simultaneously performing mesh operations, such as edge-face or octahedral swapping, Joe [1989, 1995]; Freitag and Ollivier-Gooch [1996], aimed at maintaining the Delaunay character of the mesh. Energy minimization with respect to the spatial nodal positions has the effect of equilibrating the body, whereas minimization with respect to the referential nodal positions has the effect of equilibrating the *configurational forces* acting on the nodes. Since the nodes are no longer attached to fixed material particles, the resulting finite-element method may be regarded as an r-adaption method.

This paper is concerned with the formulation of the method for static problems in nonlinear elasticity. In particular, we derive general expressions for the configuration forces for isoparametric elements under general loading. We illustrate the versatility and convergence characteristics of the method by way of selected numerical tests and applications, including the problem of a semi-infinite crack linear and nonlinear elastic bodies; and the optimization of the shape of elastic inclusions.

2 Formulation of the static problem

We consider a solid occupying a region $B \in \mathbb{R}^3$ in its reference undeformed configuration. The solid subsequently deforms under the action of externally applied forces and prescribed displacements. The deformation mapping $\boldsymbol{\varphi} : B \to \mathbb{R}^3$ maps material points $\boldsymbol{X}$ in the reference configuration into their corresponding positions $\boldsymbol{x}$ in the deformed configuration $\boldsymbol{\varphi}(B)$. The deformation gradient field follows as

$$F_{iJ} = \frac{\partial \varphi_i}{\partial X_J}, \quad \text{in } B \tag{2.1}$$

Here and subsequently, we use upper (respectively, lower) case indices to denote components of vector fields defined over the undeformed (respectively, deformed) configuration. The deformation mapping is

contrained to take a prescribed value $\bar{\boldsymbol{\varphi}}$ over the displacement part ∂B_1 of the undeformed boundary. This furnishes the boundary condition:

$$\varphi_i = \bar{\varphi}_i, \quad \text{on } \partial B_1 \tag{2.2}$$

Additionally, the solid is in equilibrium, which requires:

$$P_{iJ,J} + RB_i = 0, \quad \text{in } B \tag{2.3}$$

and

$$P_{iJ}N_J = \bar{T}_i, \quad \text{on } \partial B_2 \tag{2.4}$$

Here $\boldsymbol{P}$ denotes the first Piola-Kirchhoff stress tensor, R is the mass density per unit undeformed volume, $\boldsymbol{B}$ is the body force density per unit mass, $\boldsymbol{N}$ is the unit normal to the undeformed boundary, and $\bar{\boldsymbol{T}}$ is the applied traction over the traction boundary $\partial B_2 = \partial B - \partial B_1$. For simplicity, we shall assume that the material is elastic, with strain-energy density $W(\boldsymbol{F})$. Under these assumptions, the constitutive relations take the form:

$$P_{iJ} = \frac{\partial W}{\partial F_{iJ}}(\boldsymbol{F}) \equiv P_{iJ}(\boldsymbol{F}), \quad \text{in } B \tag{2.5}$$

With a view to formulating finite-element approximations, we begin by re-stating the preceding equations in variational form. To this end, we consider the potential energy functional

$$I[\boldsymbol{\varphi}] = \int_B W(\mathrm{Grad}\boldsymbol{\varphi})dV - \int_B R\boldsymbol{B}\cdot\boldsymbol{\varphi}dV - \int_{\partial B_2}\bar{\boldsymbol{T}}\cdot\boldsymbol{\varphi}dS \tag{2.6}$$

This functional may be discretized by the introduction of a triangulation $\mathcal{T}_h$ of B and the corresponding finite-element interpolation:

$$\boldsymbol{\varphi}_h(\boldsymbol{X}) = \sum_{a=1}^{N}\boldsymbol{x}_a N_a(\boldsymbol{X}) = \sum_{e=1}^{E}\sum_{a=1}^{n}\boldsymbol{x}_a^e N_a^e(\boldsymbol{X}) \tag{2.7}$$

where E is the number of elements, N is the number of nodes, N_a^e are the element shape functions, N_a are the nodal shape functions, and $\boldsymbol{x}_a$ are the nodal coordinates in the deformed configuration. The discrete potential energy function is

$$I_h(\boldsymbol{x}_h) = \int_B W(\mathrm{Grad}\boldsymbol{\varphi}_h)dV - \int_B R\boldsymbol{B}\cdot\boldsymbol{\varphi}_h dV - \int_{\partial B_2}\bar{\boldsymbol{T}}\cdot\boldsymbol{\varphi}_h dS \tag{2.8}$$

where $\boldsymbol{x}_h \equiv \{\boldsymbol{x}_a, a = 1,\dots,N\}$ is the array of nodal coordinates in the deformed configuration. For fixed $\mathcal{T}_h$, the finite-element solutions follow from the minimum problem

$$\inf_{\boldsymbol{x}_h} I_h(\boldsymbol{x}_h) \tag{2.9}$$

Thus, the overriding objective of the calculations is to minimize the potential energy of the body. In particular, given two approximate solutions $\boldsymbol{x}_h'$ and $\boldsymbol{x}_h''$ with $I_h(\boldsymbol{x}_h'') < I_h(\boldsymbol{x}_h')$, then $\boldsymbol{x}_h''$ is to be regarded as a *better* solution than $\boldsymbol{x}_h'$. This provides a clear and unambiguous criterion for comparing approximate solutions.

3 Static variational r-adaption method

Evidently, the energy minima attainable through the minimization process (2.9) depend on the choice of mesh. In keeping with the principle of minimum energy, the *optimal mesh is that for which the least minimum energy is achieved.* This suggests minimizing the energy with respect to both the spatial and

referential nodal coordinates. The former minimization has the effect of equilibrating the body, whereas the latter minimization has the effect of optimizing the nodal positions of the triangulation. Thus, we regard the energy I_h as a function of $\{\boldsymbol{x}_h, \boldsymbol{X}_h\}$, where $\boldsymbol{X}_h \equiv \{\boldsymbol{X}_a, a = 1, \dots, N\}$ is the array of referential nodal coordinates, and formulate the extended minimum problem

$$\inf_{\boldsymbol{x}_h, \boldsymbol{X}_h} I_h(\boldsymbol{x}_h, \boldsymbol{X}_h) \tag{3.1}$$

Since the nodes are no longer attached to fixed material particles, the resulting finite-element method may be regarded as an r-adaption method.

The stationarity of the energy now demands

$$\langle DI_h, \delta\boldsymbol{x}_h\rangle \cdot \delta\boldsymbol{x}_h + \langle DI_h, \delta\boldsymbol{X}_h\rangle \cdot \delta\boldsymbol{X}_h = 0 \tag{3.2}$$

where $\langle DI_h, \delta\boldsymbol{x}_h\rangle \cdot \delta\boldsymbol{x}_h$ and $\langle DI_h, \delta\boldsymbol{X}_h\rangle \cdot \delta\boldsymbol{X}_h$ denote the first of variations of I_h with respect to $\boldsymbol{x}_h$ and $\boldsymbol{X}_h$, respectively. Away from the displacement boundary, the variations $\delta\boldsymbol{x}_h$ and $\delta\boldsymbol{X}_h$ are independent and we obtain the Euler-Lagrange equations

$$\boldsymbol{r}_h = \frac{\partial I_h}{\partial \boldsymbol{x}_h} = 0 \tag{3.3a}$$

$$\boldsymbol{R}_h = \frac{\partial I_h}{\partial \boldsymbol{X}_h} = 0 \tag{3.3b}$$

where $\boldsymbol{r}_h$ are the out-of-balance mechanical forces at the nodes, and $\boldsymbol{R}_h$ are the corresponding out-of-balance *configurational forces*, Gurtin [1995, 2000]. The system of equations (3.3a) enforces the mechanical equilibrium of the body, whereas the system (3.3b) enforces the *configurational equilibrium* of the nodes. Jointly, eqs. (3.3a) and (3.3b) supply an extended system of equations which may be solved for the unknowns $\{\boldsymbol{x}_h, \boldsymbol{X}_h\}$.

On the displacement boundary ∂B_1, the variations $\delta\boldsymbol{x}_h$ and $\delta\boldsymbol{X}_h$ are related according to

$$\delta x_{ia} = \frac{\partial \bar{\varphi}_i}{\partial X_I}\delta X_{Ia} \tag{3.4}$$

where $\bar{\boldsymbol{\varphi}}(\boldsymbol{X})$ is the prescribed deformation on ∂B_1. Under these conditions, the corresponding configurational force equilibrium equation follows from (3.2) as

$$\frac{\partial I_h}{\partial X_{Kb}} + \frac{\partial \bar{\varphi}_k}{\partial X_K}\frac{\partial I_h}{\partial x_{kb}} = 0 \tag{3.5}$$

which replaces (3.3b) on ∂B_1.

A straightforward calculation (cf Appendix A) gives the mechanical and configurational equilibrium equations in the form

$$r_{kb} = \sum_{e=1}^{E}\left\{\int_{\Omega^e} P_{kJ}N_{b,J}dV - \int_{\Omega^e} RB_k N_b dV - \int_{\partial\Omega^e\cap\partial B_2} \bar{T}_k N_b dS\right\} = 0 \tag{3.6a}$$

$$R_{Kb} = \sum_{e=1}^{E}\int_{\Omega^e}\left\{M_{JK} + [-\bar{P}_{k,L}\varphi_{k,L} - (RB_k - \bar{P}_{kL,L})\varphi_k]\delta_{JK} + \bar{P}_{iJ}F_{iK}\right\}N_{b,J}dV = 0 \tag{3.6b}$$

where

$$M_{IJ} = W\delta_{IJ} - P_{kI}F_{kJ} \tag{3.7}$$

is Eshelby's energy-momentum tensor, and $\bar{\boldsymbol{P}}$ is any stress field such that

$$\bar{P}_{iJ}N_J = 0, \quad \text{on } \partial B_1 \tag{3.8a}$$

$$\bar{P}_{iJ}N_J = \bar{T}_i, \quad \text{on } \partial B_2 \tag{3.8b}$$

In practice, the field $\bar{\boldsymbol{P}}$ need only be one element deep. For a stable homogeneous solid in mechanical equilibrium, the configurational forces vanish identically, i. e.,

$$M_{JK,J} = 0 \tag{3.9}$$

However the introduction of a discretization breaks the translational symmetry of the body and, hence, the configurational equilibrium equations (3.3b) are not trivially satisfied in general. Indeed, eq. (3.3b) may be regarded as an additional system of equations enabling the determination of the optimal nodal coordinates X_h.

It bears emphasis that the present approach applies equally well to inelastic problems, provided that the equations of evolution are discretized in time in a variational manner, Ortiz and Stainier [1999]. In this case the functional to be minimized is incremental and depends on the initial conditions for each time step. The computation of the configurational forces is then formally identical to the elastic case explicitly treated here, with the energy-momentum tensor (3.7) expressed in terms of the effective incremental strain-energy density, Ortiz and Stainier [1999].

In solving eq. (3.3b) the movement of nodes in the reference configuration must be constrained by appropriate boundary conditions. This in turn requires an appropriate representation of the geometry and topology boundary of the domain. To this end we regard the boundary of the domain as a two-dimensional manifold without boundary comprising a number of connected components, or *shells*, Hoffmann [1989]; Mantyla [1988]; Requicha [1980]; Radovitzky and Ortiz [2000]. The shells may in turn be partitioned into smooth *faces*. The boundaries of the faces may represent salient geometric features of the shell such as ridges or sharp edges. The trivial case of a smooth shell which consists of one single face is also possible. One face may be shared by two shells, e. g., at a material boundary, in which case it appears in each shell with opposite orientations. Each face may be regarded as a 2-manifold with boundary. The boundary of a face is itself a 1-manifold without boundary. The connected components of the boundary of a face are known as *loops*. The loops may in turn be partitioned into *edges* bounded by end *vertices*. The trivial case of a smooth loop which consists of one single edge is also possible. As in the case of faces, an edge may be shared by two loops, in which case it appears in each loop with opposite orientations.

In the present implementation of the variational adaption method, we enforce the following boundary conditions:

1. Vertices are fixed points of the reference configuration.
2. Edge nodes are required to remain within their edges.
3. Face nodes are required to remain within their faces.

These boundary conditions are chosen so as to preserve the boundary representation of the solid. However, it should be noted that these boundary conditions constrain the number of nodes within boundary faces and edges to remain constant, which in turn limits the range of attainable meshes. A more general and flexible approach would allow for nodes to move in and out of edges and faces, but these extensions will not be pursued here.

So far, we have envisioned the minimization of the energy with respect to the nodal coordinates of a *fixed* triangulation. However, keeping the triangulation fixed introduces topological constraints which may be too restrictive in general. A more flexible approach, which we adopt in calculations, consists of allowing for variations in the triangulation as part of the mesh optimization process. This suggests the more general problem:

Problem: Find the triangulation, nodal coordinates and nodal displacements which minimize the energy.

However, the exact optimization of the triangulation based on energy minimization constitutes a discrete problem which entails great difficulty. As a compromise, we combine the equilibrium iterations with ad-hoc 'mesh-improvement' operations such as edge-face or octahedral swapping, Joe [1989, 1995]; Freitag and Ollivier-Gooch [1996]. While these operations do not necessarily lead to optimal meshes in the sense of energy minimization, they enable the free migration of nodes without mesh entanglement, thus making meshes attainable which otherwise could not be reached from the initial mesh.

4 Static examples

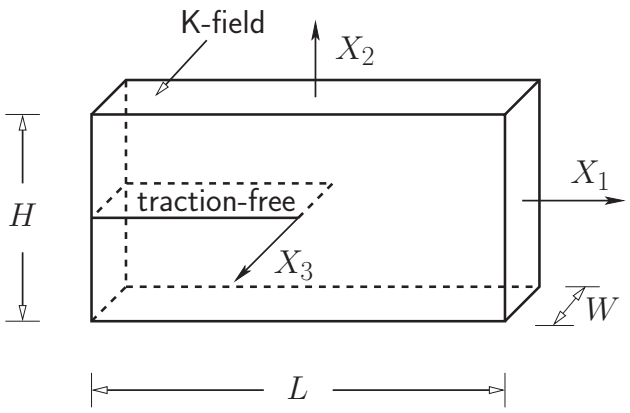

Figure 4.1: Geometry of the mode-I fracture problem considered in the convergence study.

In this section we present test cases which illustrate the convergence characteristics of the method. The particular configuration under consideration concerns a semi-infinite crack in an infinite elastic solid subjected to mode I opening, Fig. 4.1. This test is exacting in that it involves the strongest singularity that can be sustained by a linear elastic solid. In addition, when applied to linear elastic solids the test is particularly convenient due to the availability of an exact analytical solution, which in conjunction with the normed-space structure of the space of solutions, namely the Sobolev space of functions $H^1(\Omega, \mathbb{R}^n)$, permits the computation of global error norms.

The calculations presented here employ a loop-in-loop Polak-Ribiere iterative solution procedure, Shewchuk [1994]. This solution procedure consists of two nested iterative loops: an outer loop for the nodal coordinates in the reference configuration, driven by (3.6b); and an inner loop for the nodal displacements, at fixed nodal coordinates, driven by (3.6a). In this scheme, the nodal configurational forces are always computed from equilibrated displacement fields. Failure to comply with this condition may result in inadmissible mesh geometries, e. g., meshes including inverted elements. In addition to the double iteration for nodal coordinates and displacements, mesh-improvement operations are periodically performed in order to avoid mesh entanglement and allow for transitions in the mesh topology.

4.1 Two-dimensional linear elastic crack

Fig. 4.2 shows the mesh resulting from the application of the method to the two-dimensional plane-strain problem. The computational domain consists of a rectangular region in the upper half plane, with traction-free boundary conditions enforced on the crack flank, symmetry boundary conditions imposed on the crack

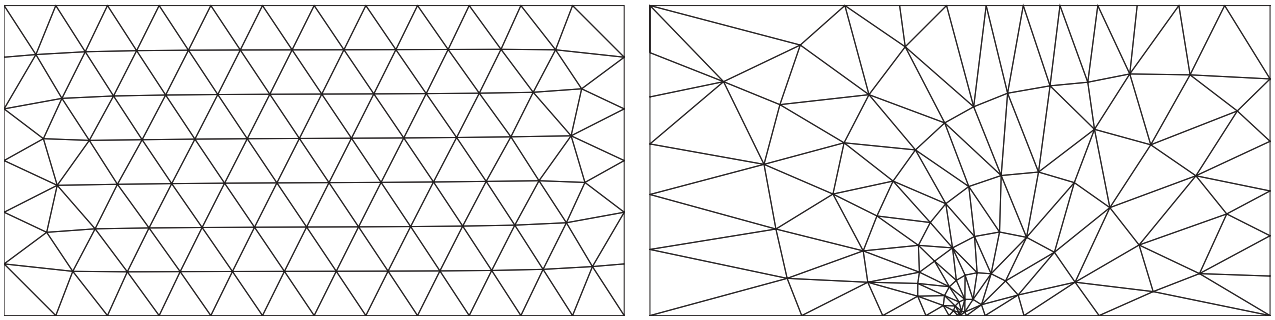

(a) (b)

Figure 4.2: Two-dimensional analysis of a semi-infinite crack in a linear elastic solid subjected to mode I loading. The computational mesh consists of 166 three-node elements. Evolution of mesh: a) Initial uniform mesh; b) Optimal mesh focused at the crack tip.

	$\| \boldsymbol{u}_h - \boldsymbol{u} \|_0$	$\lvert \boldsymbol{u}_h - \boldsymbol{u} \rvert_E$
without mesh adaption	0.8794	0.5172
with mesh adaption	1.1369	0.6662

Table 1: Two-dimensional analysis of a semi-infinite crack in a linear elastic solid subjected to mode-I loading.

ligament, and the mode I displacement K-field prescribed on the remainder of the boundary. The crack tip is regarded as a vertex in the boundary representation and, in consequence, it is held fixed in the reference configuration during the relaxation of the mesh. The Poisson ratio of the solid is $\nu = 0.3$. The computational mesh consists of three-node linear triangular elements.

Fig. 4.2a shows an initial mesh comprising 166 elements and Fig. 4.2b the final mesh after the application of the method. As expected, energy minimization drives *both* mesh refinement near the crack tip and unrefinement elsewhere. The combination of nodal relaxation and edge swapping results in a *relaxed Delaunay mesh*, i. e., a mesh in which all nodes are in configurational equilibrium and all elements satisfy the Delaunay circumcircle condition. It should also be carefully noted that edge-swapping results in a complete reconstruction of the mesh connectivity, or topology. This reconstruction is critical in order to allow the migration of nodes towards the crack tip without mesh entanglement. It also bears emphasis that the mesh adaption shown in Fig. 4.2b is accomplished *without resorting to error estimates or mesh adaption indicators*. Indeed, the entire solution follows directly from the variational principle.

Fig. 4.3 shows the dependence of the displacement L^2 and energy-norm error of the variationally adapted and uniform mesh solutions on the average mesh size, defined as $h \sim \sqrt{|\Omega|/E}$, where $|\Omega|$ is the area of the domain of analysis and E is the number of elements. The error norms are normalized by the corresponding norm of the exact solution. In addition, the convergence rates deduced from these plots are collected in Table 1. The convergence rate is the logarithmic derivative of the error *vs* mesh-size curve asymptotically as $h \to 0$. The computed convergence rates suggest that the variational adaption method speeds up the rate of convergence, and substantially lowers the error, relative to the uniform-mesh solution.

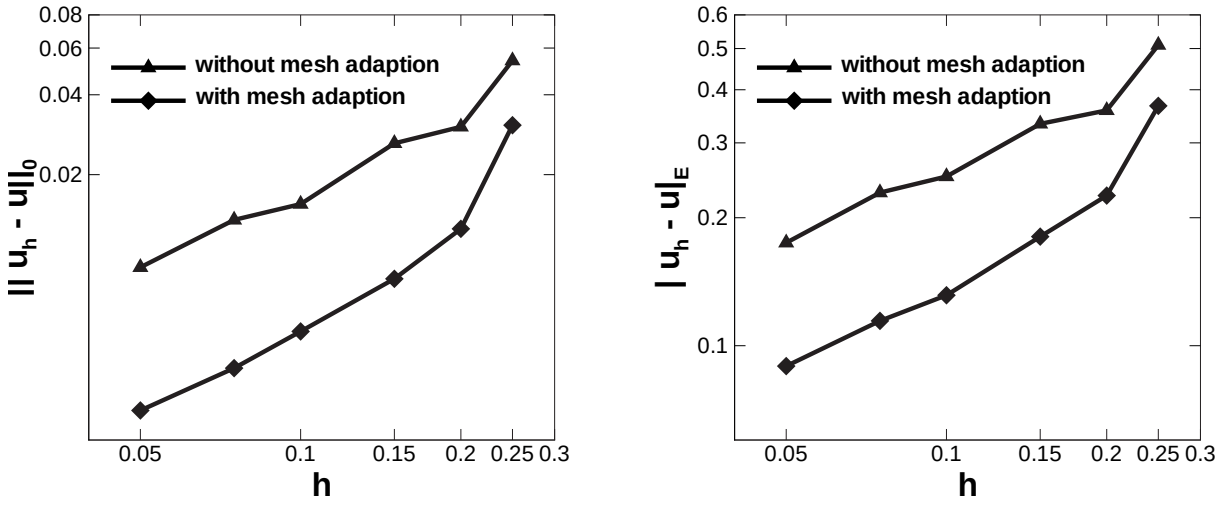

(a) (b)

Figure 4.3: Two-dimensional analysis of a semi-infinite crack in a linear elastic solid subjected to mode I loading, convergence plots: a) L^2-norm of displacement error; b) Energy norm of displacement error.

	$\| \boldsymbol{u}_h - \boldsymbol{u} \|_0$	$\lvert \boldsymbol{u}_h - \boldsymbol{u} \rvert_E$
without mesh adaption	0.8400	0.3993
with mesh adaption	0.8952	0.4181

Table 2: Three-dimensional analysis of a semi-infinite crack in a linear elastic solid subjected to mode I loading, convergence rates.

4.2 Three-dimensional linear elastic crack

As a three-dimensional example of application of the method, the problem discussed in the preceding section may also be solved on a plate of finite thickness by constraining the normal displacements on the faces perpendicular to the crack front in order to enforce plain-strain conditions. All calculations presented here employ four-node linear tetrahedral elements. The application of mesh-improvement operations in a manner that preserves the integrity of the boundary representation is greatly compounded in three dimensions. The construction of three-dimensional *contrained* Delaunay triangulations which properly restrict to a prescribed boundary is a difficult and largely open problem, Amenta and Bern [1999]; Radovitzky and Ortiz [2000]; Sampl [2001]; Amenta et al. [2002]. In the problem under consideration, the main difficulty resides in ensuring that the mesh operations preserve the geometry of the crack front. Here we sidestep these difficulties by the simple device of scaling down the thickness of the plate prior to the application of the mesh operations. The scaled thickness is chosen to be much smaller than the size of the smallest element in the mesh. The plate is then restored to its actual thickness following the application of the mesh operations.

Fig. 4.4 depicts the evolution of the mesh, Fig. 4.5 shows the computed convergence plots, and Table 2 collects the computed convergence rates. As in the two-dimensional case, the initially uniform mesh is refined near the tip and unrefined elsewhere. The computed convergence rates again suggest that the varia-

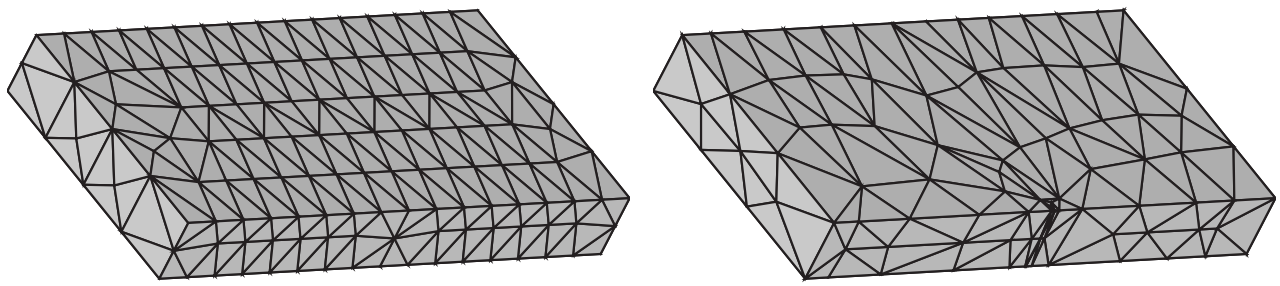

(a) (b)

Figure 4.4: Three-dimensional analysis of a semi-infinite crack in a linear elastic solid subjected to mode I loading. The computational mesh consists of 493 three-node elements. Evolution of mesh: a) Initial uniform mesh; b) Optimal mesh focused at the crack tip.

tional adaption method speeds up the rate of convergence, and substantially lowers the error, relative to the uniform-mesh solution.

4.3 Two-dimensional crack in a neo-Hookean solid

Next we demonstrate the applicability of the method to nonlinear problems by revisiting the problem presented in Section 4.1 and considering a crack in a compressible neo-Hookean solid characterized by the strain-energy density

$$W(\boldsymbol{F}) = \frac{1}{2}\lambda_0 \log^2(J) - \mu_0 \log(J) + \frac{\mu_0}{2}\mathrm{tr}(\boldsymbol{F}^T\boldsymbol{F}) \tag{4.1}$$

where λ_0 and μ_0 are material constants and $J = \det(\boldsymbol{F})$ is the Jacobian of the deformation. For this material, the first Piola-Kirchhoff stress follows as

$$\boldsymbol{P} = \lambda_0 \log(J)\boldsymbol{F}^{-T} + \mu_0(\boldsymbol{F} - \boldsymbol{F}^{-T}) \tag{4.2}$$

The material constants used in calculations are $\lambda_0 = 1.255 \times 10^8$ and $\mu_0 = 8.365 \times 10^7$, corresponding to an undeformed Young's modulus $E_0 = 2.175 \times 10^8$ and Poisson's ration $\nu_0 = 0.3$.

Fig. 4.6a shows an initial uniform mesh comprising 166 elements, and Fig. 4.6b the final mesh after the application of the variational adaption method. As before, energy minimization drives both mesh refinement near the crack tip and coarsening elsewhere. As argued in the introduction, owing to the finite kinematics involved in this problem, there is no natural norm that provides a measure of the numerical error, and convergence should be understood directly in terms of the energy of the system. Fig. 4.7 shows the dependence of the energy, computed with and without adaption, on the mesh size. As is evident from the figure, the energy

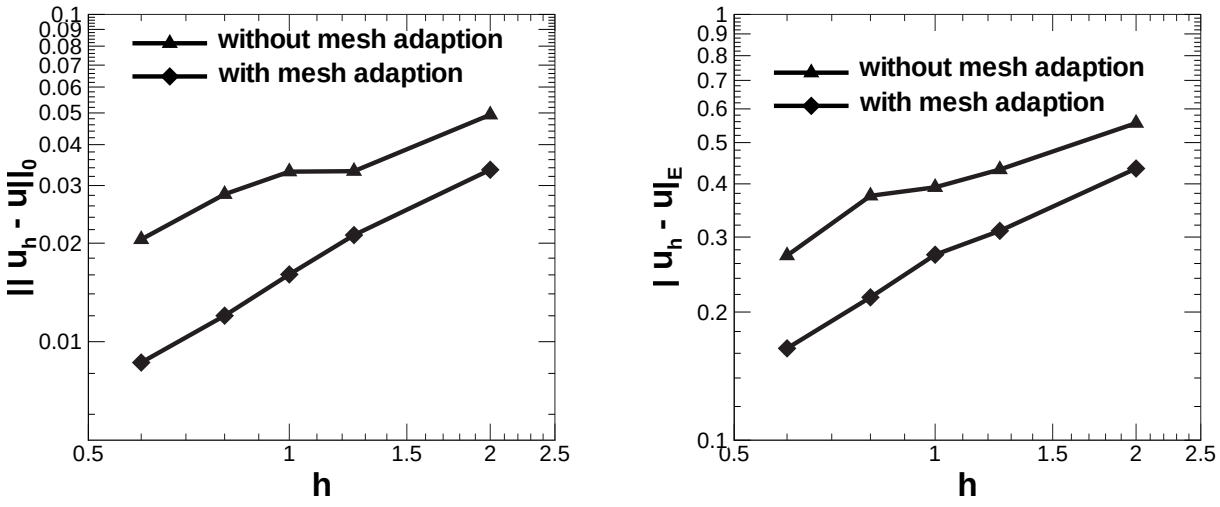

(a) (b)

Figure 4.5: Three-dimensional analysis of a semi-infinite crack in a linear elastic solid subjected to mode I loading, convergence plots: a) L^2-norm of displacement error; b) Energy norm of displacement error.

ostensibly converges as the mesh size decreases to zero. As expected, the energy obtained by relaxing the mesh is smaller–and appears to approach the exact energy faster–than the energy of the uniform mesh.

In the above calculations optimal meshes have been obtained for a fixed number of nodes. Evidently, the minimum energy attainable under such conditions is limited by the number of nodes, and further energy reduction requires the insertion of nodes into the mesh. Nodes could be inserted simply by a variety of means, e. g., by placing new nodes at the barycenter of all or selected elements, followed by energy minimization and mesh reconnection for the new nodal set. The opposite operation of reducing the number of nodes may also be accomplished by a variety of means, e. g., by element collapse Molinari and Ortiz [2002]. However, the optimal strategy for adding and removing nodes, and for allowing nodes to migrate in and out of the boundary of the domain, is not clear at present and these extensions will not be pursued here.

4.4 Nodal energy-release rate

An added benefit of the variational adaption approach is that it supplies, *as nodal values*, the configurational or energetic forces acting on boundaries and interfaces. In particular, it supplies the nodal values of the energy-release rate on the nodes of a crack-front. Thus, since the crack-tip node is held fixed during the relaxation of the mesh, the configurational force acting on it does not vanish at equilibrium. Indeed, this unbalanced configurational force is the energetic force conjugate to the position of the crack, i. e., the rate of release of elastic energy per unit crack advance, or *energy-release rate*. The energy-release rate may be computed or estimated by a number of other means, including compliance methods, e. g., Kanninen and Popelar [1985], and the J-integral, Rice [1968]; Shih and Nakamura [1986]; Moran and Shih [1987].

In two dimensions, the energy-release rate is

$$G_h = -\frac{\partial I_h}{\partial a} = -R \tag{4.3}$$

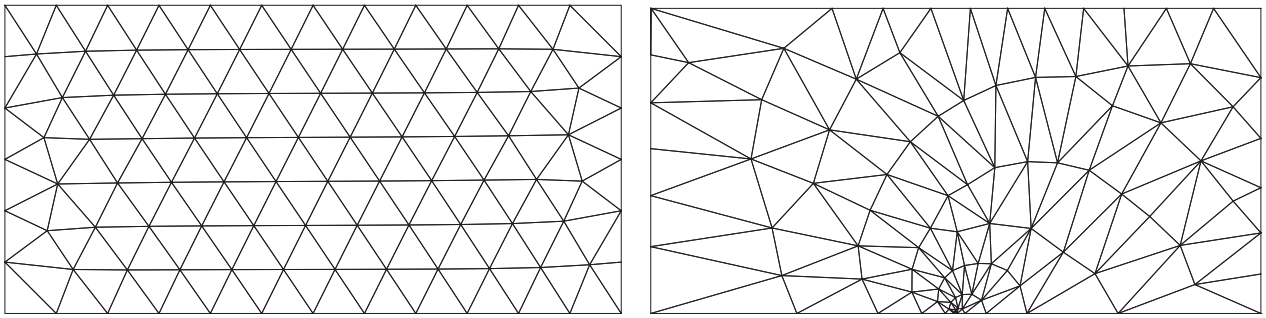

(a) (b)

Figure 4.6: Two-dimensional analysis of a semi-infinite crack in a neo-Hookean elastic solid subjected to mode I loading. The computational mesh consists of 166 three-node elements. Evolution of mesh: a) Initial uniform mesh; b) Optimal mesh focused at the crack tip.

where a is the crack length and R follows by specializing (3.6b) to the crack-tip node and the crack-wise coordinate direction. Fig. 4.8 shows the dependence of G_h on the average mesh size as computed in the two-dimensional linear-elastic crack problem, Section 4.1. Also shown for comparison is the exact value of the energy-release rate, e. g., Rice [1968],

$$G = \frac{1-\nu^2}{E} K^2 \tag{4.4}$$

where K is the mode-I stress intensity factor, ν is Poisson's ratio and E is Young's modulus. As is evident from the figure, the numerical energy-release rate matches the exact value to within good accuracy even for relatively coarse meshes.

The connection between crack-tip nodal configurational forces and energy-release rates was explicitly recognized by Sussman and Bathe [1985]. This connection is also implied in methods which compute the energy-release rate by perturbing the position of the crack front, Parks [1974]. Methods which compute the energy-release rate as a nodal configuration force necessarily result in expressions which are special cases of eq. (3.6b). An expression consistent with eq. (3.6b) can also be recovered from the volume-integral version of the J-integral, Li et al. [1985]; Shih and Nakamura [1986]; Moran and Shih [1987], by choosing the integration volume to coincide with the ring of elements incident on a crack-tip node and additionally choosing the weight-function to coincide with the shape-function for that node. As noted earlier, the present approach for the computation of configurational forces applies equally well to inelastic problems, provided that the equations of evolution are discretized in time in a variational manner, Ortiz and Stainier [1999].

5 Application to shape optimization

In all the preceding calculations, the relaxation of the mesh has been subjected to constraints introduced in order to preserve the geometry of the model. For instance, the nodes may be constrained to move within boundaries and interfaces in the reference configuration, which has the effect of leaving the geometry of those objects invariant. By simply removing these geometrical constraints, then the variational adaption method may be used to compute *equilibrium shapes*, i. e., shapes of boundaries and interfaces which minimize the energy of the system. The salient attributes of the approach are: the finite-element mesh directly

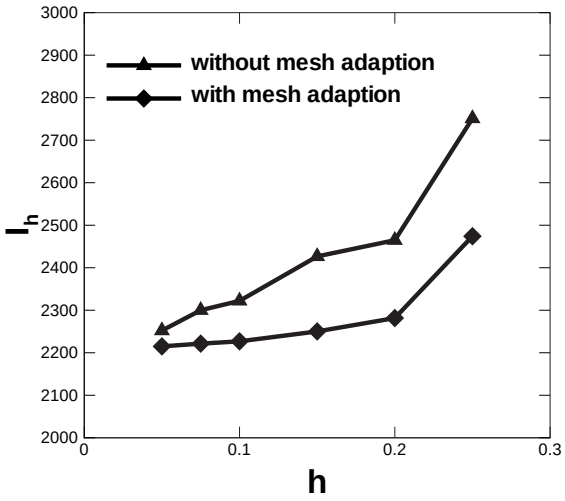

Figure 4.7: Two-dimensional analysis of a semi-infinite crack in a neo-Hookean elastic solid subjected to mode I loading. Energy *vs* mesh size for uniform and relaxed meshes.

supplies the geometrical representation of the system; the equilibration of configurational forces optimizes the mesh and the geometry of the system simultaneously; and the approach allows for arbitrary material behavior, including anisotropy and nonlinearity.

By way of illustration we specifically consider the problem of determining the equilibrium shape of an elastic inclusion, e. g., a second-phase particle or a precipitate, embedded in a likewise elastic matrix. Our aim here is merely to illustrate how the variational adaption method can be applied to problems of shape optimization. A comprehensive study of the mechanics of symmetry-breaking transitions or the behavior of specific materials is beyond the scope of this work and may be found elsewhere (see, e. g., Voorhees [1985]; Voorhees et al. [1988]; Voorhees [1992]; Voorhees et al. [1992]; Jou et al. [1997]; Leo et al. [2000, 2001], and references therein). Alternative approaches to shape optimization may also be found elsewhere (e. g., Maute and Ramm [1995, 1997]; Bendsoe and Kikuchi [1988]; Leo et al. [1998]; Maute et al. [1999]; Schleupen et al. [2000]; Jog et al. [2000]; Hou et al. [2001]; Schwarz et al. [2001]).

A simple form of the energy of the inclusion/matrix system is

$$I = \int_B W(\mathrm{Grad}\boldsymbol{\varphi})dV + \int_\Gamma \gamma dS + \frac{\alpha}{2}\left(V_2 - \int_{B_2} dV\right)^2 \tag{5.1}$$

where B_2 is domain of the precipitate, $B_1 = B - B_2$ the domain of the matrix, Γ is the interface between the precipitate and the matrix, γ is the interface energy density for interface, V_2 volume of the precipitate, and α a penalty parameter. For simplicity we take the interfacial energy to be isotropic. Upon discretization, the energy function is

$$I_h = \int_B W(\mathrm{Grad}\boldsymbol{\varphi}_h)dV + \int_\Gamma \gamma dS + \frac{\alpha}{2}\left(V_2 - \int_{B_2} dV\right)^2 \equiv I_h^{\mathrm{mat}} + I_h^{\mathrm{int}} + I_h^{\mathrm{vol}} \tag{5.2}$$

which, as before, is to be regarded as a function of the nodal coordinates $\boldsymbol{x}_h$ and $\boldsymbol{X}_h$ in the deformed and undeformed configurations, respectively. The equilibrium shape of the precipitate now follows by minimization of I_h with respect to $\{\boldsymbol{x}_h, \boldsymbol{X}_h\}$. The stationarity condition is again of the form (3.2), and the

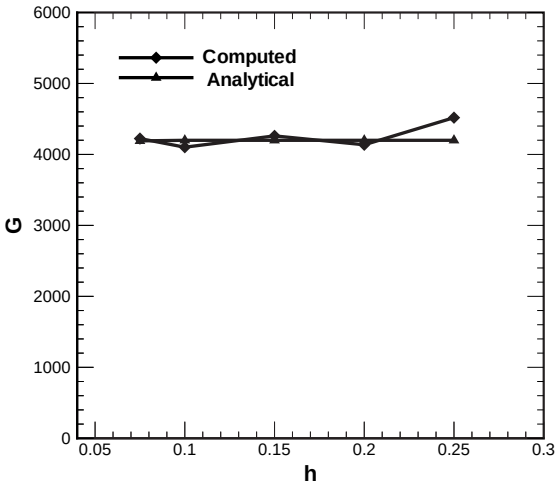

Figure 4.8: Mesh-size dependence of the energy-release rate for a mode-I linear-elastic crack computed as a nodal configurational force. The exact value is also shown for comparison.

corresponding Euler-Lagrange equations of the form (3.3a) and (3.3b), but now the configurational forces have additional structure arising from the interfacial energy, $I_h^{\rm int}$, and the volume constraint energy, $I_h^{\rm vol}$. Thus, we have

$$R_{bK} = R_{bK}^{\rm mat} + R_{bK}^{\rm int} + R_{bK}^{\rm vol} \tag{5.3}$$

where each of the terms on the right hand side follows by differentiation of the corresponding energy term with respect to $\boldsymbol{X}_h$. Evidently, $R_{bK}^{\rm mat}$ is a special case of (3.6b). The remaining terms are evaluated in Appendix B.

By way of numerical example, we consider the case of an isolated linear elastic cylindrical inclusion coherently embedded in a likewise linear elastic matrix of infinite extent undergoing plane-strain deformation. The problem of two phases of Young's moduli $E^{\rm inc}$ and $E^{\rm mat}$ and a common Poisson's ratio of ν, where in addition the inclusion undergoes a dilatational misfit strain of ϵ^* and the interface has surface energy γ, has been studied analytically by Johnson and Cahn [1984]. The elastic strain energy scales with the inclusion volume and favors an elliptic shape. By contrast, the surface energy scales with the interfacial area and favors a circular shape. By virtue of this competition, the equilibrium shape of the inclusion depends on its volume. Thus, for small inclusions, the surface to volume ratio is large and the inclusion shape is dominated by the interfacial energy, resulting in ostensibly circular shapes. By contrast, for large inclusions the surface to volume ratio is small and the inclusion shape is dominated by the strain energy, which results in elliptic shapes. The transition from one regime to the other occurs at the critical radius, Johnson and Cahn [1984],

$$r_c = \frac{3(1+\delta-2\nu)^2(1+\kappa\delta)\gamma}{4\mu^{\rm inc}\delta(1-\delta)(1+\kappa)\epsilon^{*2}} \tag{5.4}$$

where $\kappa = 3-4\nu$, $\delta = \mu^{\rm inc}/\mu^{\rm mat}$ and μ is the shear modulus.

5.1 Isotropic inclusion and matrix

In calculations we take $E^{\rm inc} = 100$ GPa, $E^{\rm mat} = 150$ GPa, $\nu = 1/3$, $\epsilon^* = 0.01$, and $\gamma = 50$ mJ/m^2. For these values of the parameters the critical radius is $r_c = 35.62$ nm. Owing to the two-fold symmetry of

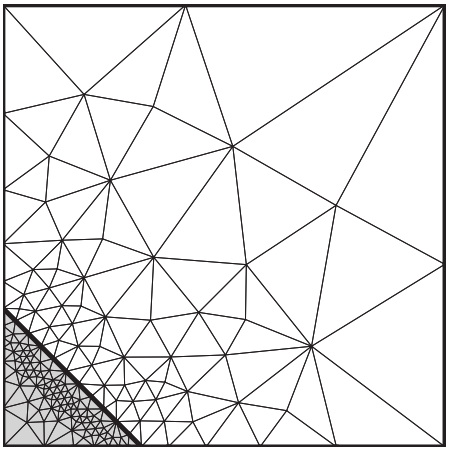

Figure 5.1: Initial inclusion shape and finite-element mesh adopted in the computation of the equilibrium shapes of inclusions.

the system the computational domain may be reduced to one single quadrant. The initial mesh used in the calculations is shown in Fig. 5.1 and consists of linear triangular elements.

The computed equilibrium shapes for inclusions of sizes $r = 31.91$ nm $< r_c$, and $r = 39.89$ nm $> r_c$, are shown in Fig. 5.2, which also displays the analytical equilibrium shapes for comparison, Johnson and Cahn [1984]. As is evident from the figure, the computed equilibrium shapes are in close agreement with the corresponding analytical solutions. In particular, the small inclusion adopts a spherical shape at equilibrium, whereas the large inclusion adopts an elliptical shape, in keeping with the stability analysis of Johnson and Cahn [1984].

5.2 Cubic inclusion and matrix

Next we consider cubic phases of elastic moduli $C_{11} = 200$ GPa, $C_{12} = 100$ GPa, and $C_{44} = 150$ GPa, a misfit strain $\epsilon^* = 0.01$ in the inclusion, a surface energy $\gamma = 50$ mJ/m^2, and an inclusion size of 40nm. Fig. 5.3 shows the computed equilibrium shape of the inclusion, which is closer to a square shape than in the isotropic case. Although no analytical solution appears to be in existence for this problem, the computed equilibrium shape is in close agreement with those computed by other methods by Jog et al. [2000], Thomson and Voorhees [1994], and Schmidt and Gross [1997].

6 Conclusions

We have developed a variational r-adaption method for static problems. The distinguishing characteristic of this method is that it relies on the variational principle to simultaneously supply the solution, the optimal mesh and, in problems of shape optimization, the equilibrium shapes of the system. This is accomplished by minimizing the energy functional with respect to the nodal field values as well as with respect to the triangulation of the domain of analysis. Energy minimization with respect to the field variables has the effect of equilibrating the body, whereas energy minimization with respect to the referential nodal positions has the effect of equilibrating the energetic or *configurational forces* acting on the nodes.

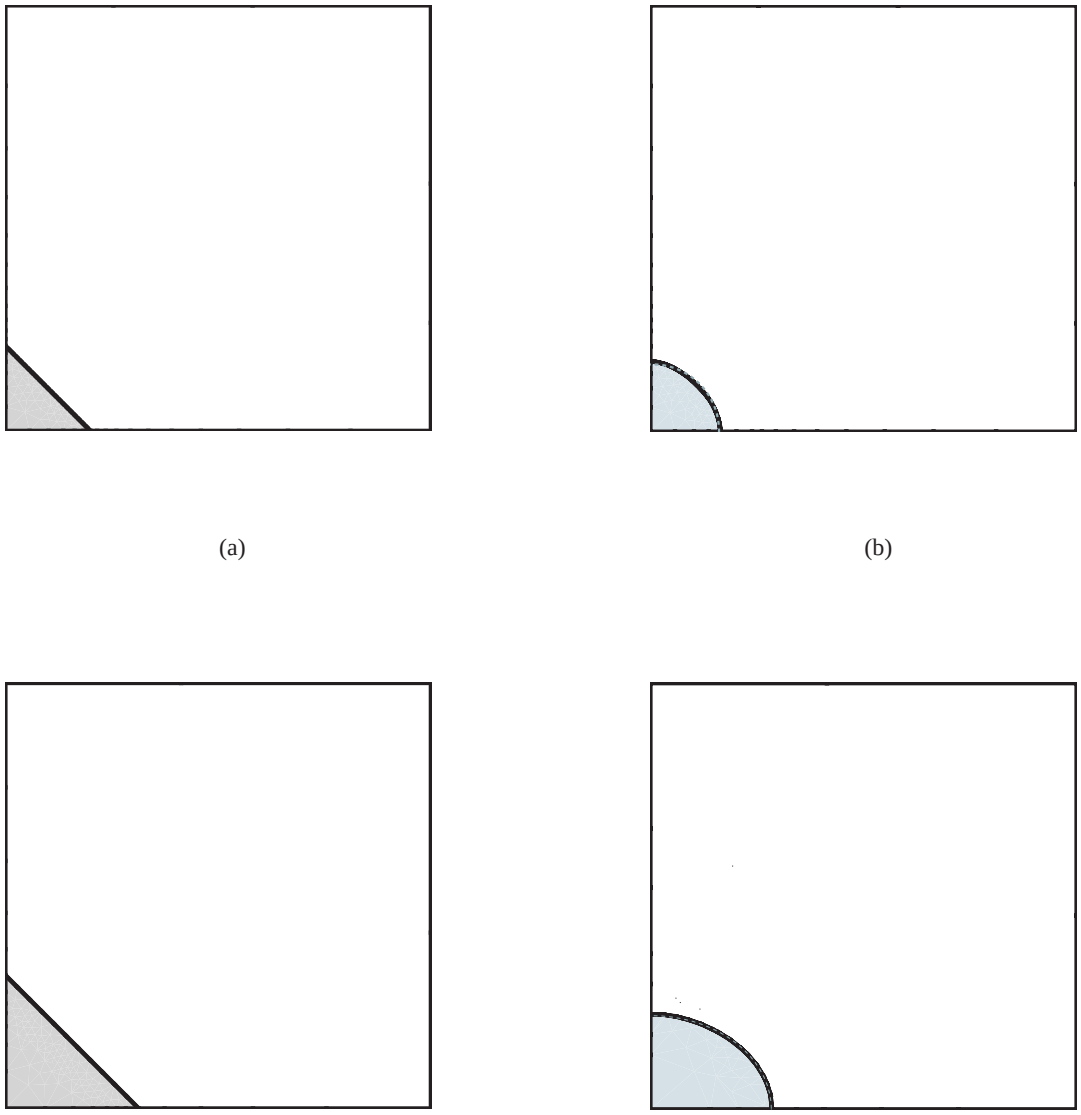

(a) (b)

(c) (d)

Figure 5.2: Equilibrium shapes an isotropic inclusion/matrix system, $E^{\mathrm{inc}} = 100$ GPa, $E^{\mathrm{mat}} = 150$ GPa, $\nu = 1/3$, $\epsilon^* = 0.01$, $\gamma = 50$ mJ/m^2, and $r_c = 35.62$ nm. a) Initial shape of small ($r = 31.91$ nm $< r_c$) inclusion. b) Computed and analytical (red) equilibrium shape of small inclusion. c) Initial shape of large ($r = 39.89$ nm $> r_c$) inclusion. d) Computed and analytical (red) equilibrium shape of large inclusion.

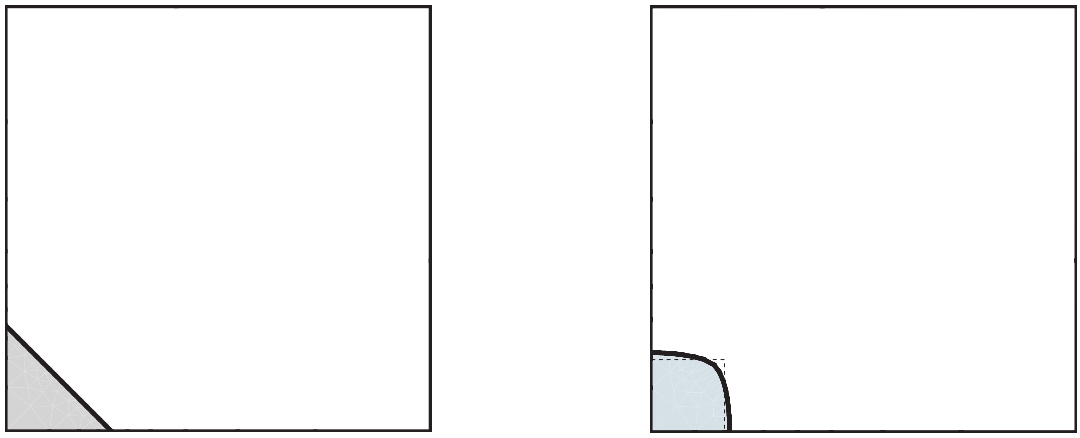

(a) (b)

Figure 5.3: Equilibrium shapes a cubic inclusion/matrix system, $C_{11} = 200$ GPa, $C_{12} = 100$ GPa, and $C_{44} = 150$ GPa, $\epsilon^* = 0.01$, $\gamma = 50$ mJ/m^2. a) Initial shape of a 40 nm inclusion. b) Computed equilibrium shape of the inclusion.

An appealing aspect of the variational adaption method is that mesh optimization, including both refinement and unrefinement, is achieved *without resorting to error estimates or mesh adaption indicators*. Indeed, the entire solution, namely, the triangulation and the field variables, emanates directly from the variational principle. This confers the variational adaption method great simplicity in comparison with traditional methods based on error estimation and minimization. Another limitation of traditional methods is that they rely strongly on error bounds expressed in terms of norms. Such error bounds are known with any degree of generality only for linear elliptic problems, and are difficult to implement in practice. More worrisome is the reliance of traditional methods on a linear functional space structure. Whereas for linear elliptic problems the energy supplies a natural norm and the space of solutions possesses a natural linear structure, no such natural linear structure exists for general *nonlinear* problems, especially where finite kinematics is concerned. By contrast, *the energy of the system always makes mathematical and physical sense*, regardless of the linearity or nonlinearity of the problem.

It is also noteworthy that, by virtue of the application of mesh improvement operations, the mesh connectivity, or topology, is reconstructed during the relaxation of the mesh. This flexibility is essential in order for arbitrary variations in mesh density to be possible. For instance, in the semi-infinite crack example treated in Section 4, a dynamic reconstruction of the mesh connectivity enables the nodes to migrate towards the crack tip unimpeded. The limitations of the present implementation are also evident in that example. Thus, for instance, in order to maintain the integrity of the boundary representation of the computational domain, the number of nodes on all edges and faces of the boundary is held fixed. These constraints limit the evolution of the mesh, e. g., by limiting the extent of refinement or unrefinement near the boundary. The lack of an optimal ratio of boundary to interior nodes may in turn result in elongated elements, such as are evident in Fig. 4.4, and generally detract from the quality of the mesh. A worthwhile extension of the method would consist of allowing nodes to move in and out of boundary edges and faces in accordance with the energetics of the system.

Acknowledgements

Support from the DoE through Caltech's ASCI/ASAP Center for the Simulation of the Dynamic Response of Solids, and from the ONR grant number NOOO14-96-1-0068, is gratefully acknowledged.

A Configurational forces for isoparametric elements

In this appendix we derive explicit expressions for the nodal configurational forces for isoparametric elements. Begin by expressing the discrete energy in the form

$$I_h = \sum_{e=1}^{E} \left\{ \int_{\Omega^e} W(\mathrm{Grad}\boldsymbol{\varphi}_h) dV - \int_{\Omega^e} R\boldsymbol{B}\cdot\boldsymbol{\varphi}_h dV - \int_{\partial\Omega^e\cap\partial B_2} \bar{\boldsymbol{T}}\cdot\boldsymbol{\varphi}_h dS \right\} \equiv I_h^{(1)} - I_h^{(2)} - I_h^{(3)} \tag{A.1}$$

where E is the number of elements and Ω^e is the undeformed domain of element e. Next we compute the variations of each of the terms in Eq. A.1 with respect to $\boldsymbol{X}_h$, for the particular case of isoparametric interpolation, i. e., for local shape functions of the form

$$N_a^e = \hat{N}_a \circ \boldsymbol{\eta}^{e-1} \tag{A.2}$$

where

$$\boldsymbol{\eta}^e(\hat{\boldsymbol{X}}) = \sum_{a=1}^{n} \boldsymbol{X}_a^e \hat{N}_a(\hat{\boldsymbol{X}}) \tag{A.3}$$

is the isoparametric mapping for element e, defined over the standard domain $\hat{\Omega}$ of the element, and $\boldsymbol{X}_a^e$ are the nodal coordinates in the undeformed configuration of the element. Begin by writing

$$I_h^{(1)} = \sum_{e=1}^{E} \int_{\hat{\Omega}} W \left(\sum_{a=1}^{n} x_{ia} \hat{N}_{a,A} \frac{\partial \hat{X}_A}{\partial X_J} \right) \det(\hat{\nabla}\boldsymbol{\eta}^e) d\hat{\Omega} \tag{A.4}$$

Taking variations with respect to $\delta\boldsymbol{X}_h$ gives:

$$\begin{aligned} \delta I_h^{(1)} = \sum_{e=1}^{E} \int_{\hat{\Omega}} \Bigg\{ & -P_{iJ} \left[\sum_{a=1}^{n} x_{ia} \hat{N}_{a,A} \frac{\partial \hat{X}_A}{\partial X_K} \left(\sum_{b=1}^{n} \delta X_{bK}^e \hat{N}_{b,B} \right) \frac{\partial \hat{X}_B}{\partial X_J} \right] \\ & + W \left(\sum_{b=1}^{n} \delta X_{bK}^e \hat{N}_{b,B} \right) \frac{\partial \hat{X}_B}{\partial X_K} \Bigg\} \det(\hat{\nabla}\boldsymbol{\eta}^e) d\hat{\Omega} \end{aligned} \tag{A.5}$$

or

$$\delta I_h^{(1)} = \sum_{e=1}^{E} \int_{\Omega^e} M_{JK} \left(\sum_{b=1}^{n} \delta X_{bK}^e N_{b,J} \right) dV \tag{A.6}$$

where

$$M_{JK} = W\delta_{JK} - F_{iK}P_{iJ} \tag{A.7}$$

is Eshelby's energy-momentum tensor, Eshelby [1975]. In addition we have

$$I_h^{(2)} = \sum_{e=1}^{E} \int_{\hat{\Omega}} RB_i \left(\sum_{a=1}^{n} x_{ia} \hat{N}_a \right) \det(\hat{\nabla}\boldsymbol{\eta}^e) d\hat{\Omega} \tag{A.8}$$

Taking variations we obtain

$$\delta I_h^{(2)} = \sum_{e=1}^{E} \int_{\hat{\Omega}} RB_i \left(\sum_{a=1}^{n} x_{ia} \hat{N}_a \right) \left(\sum_{b=1}^{n} \delta X_{bK}^e \hat{N}_{b,B} \right) \frac{\partial \hat{X}_B}{\partial X_K} \det(\hat{\nabla} \boldsymbol{\eta}^e) d\hat{\Omega} \tag{A.9}$$

or

$$\delta I_h^{(2)} = \sum_{e=1}^{E} \int_{\hat{\Omega}} RB_i \varphi_i \left(\sum_{b=1}^{n} \delta X_{bK}^e N_{b,K} \right) dV \tag{A.10}$$

Finally we turn to the traction term. To this end, let $\bar{\boldsymbol{P}}$ be any tensor-valued function such that $\bar{P}_{iJ} N_J = \bar{T}_i$ on ∂B_2 and $\bar{P}_{iJ} N_J = 0$ on ∂B_1. In practice, the function $\bar{\boldsymbol{P}}$ need only be one element deep. Then we have

$$I_h^{(3)} = \int_{\partial B} \bar{P}_{iJ} N_J \varphi_i dS = \int_B (\bar{P}_{iJ} \varphi_i)_{,J} \, dV = \int_B (\bar{P}_{iJ} \varphi_{i,J} + \bar{P}_{iJ,J} \varphi) dV \tag{A.11}$$

Each of the two term in the last expression can now be given a treatment identical to the terms $I_h^{(1)}$ and $I_h^{(2)}$ discussed earlier. Collecting all terms we obtain

$$\delta I_h = \sum_{e=1}^{E} \int_{\Omega^e} \left\{ [W - \bar{P}_{k,L} \varphi_{k,L} - (RB_k - \bar{P}_{kL,L}) \varphi_k] \delta_{JK} - (P_{iJ} - \bar{P}_{iJ}) F_{iK} \right\} \left(\sum_{b=1}^{n} \delta X_{bK}^e N_{b,J} \right) dV \tag{A.12}$$

Collecting terms, the nodal configurational force follows as

$$R_{Kb} = \frac{\partial I_h}{\partial X_{Kb}} = \sum_{e=1}^{E} \int_{\Omega^e} \left\{ M_{KJ} + [-\bar{P}_{k,L} \varphi_{k,L} - (RB_k - \bar{P}_{kL,L}) \varphi_k] \delta_{JK} + \bar{P}_{iJ} F_{iK} \right\} N_{b,J} dV \tag{A.13}$$

B Configurational forces for interface optimization

In optimizing the shape of elastic inclusions the energy needs to be augmented by the addition of interfacial and volume constraint terms. For simplicity, we consider the case of constant and isotropic surface energy, and finite elements whose restrictions to the interfaces to be optimized define a collection of surface isoparametric elements $\{\Gamma^e, e = 1, \ldots, S\}$. Thus, for every element e, the isoparametric mapping

$$\boldsymbol{X} = \boldsymbol{\eta}^e(\hat{X}_1, \hat{X}_2) \tag{B.1}$$

maps the standard domain $\hat{\Gamma}$ into the actual domain Γ^e of the element in $\mathbb{R}^3$. Here $(\hat{X}_1, \hat{X}_2)$ are parametric coordinates defined on $\hat{\Gamma}$. Under these assumptions, the interfacial energy takes the form

$$I_h^{\text{int}} = \sum_{e=1}^{S} \int_{\hat{\Gamma}} \gamma \, |\boldsymbol{\eta}_{,1}^e \times \boldsymbol{\eta}_{,2}^e| \, d\hat{\Gamma} \tag{B.2}$$

Taking variations we obtain

$$\delta I_h^{\text{int}} = \sum_{e=1}^{S} \int_{\hat{\Gamma}} \gamma \, \frac{(\boldsymbol{\eta}_{,1}^e \times \boldsymbol{\eta}_{,2}^e)_I}{|\boldsymbol{\eta}_{,1}^e \times \boldsymbol{\eta}_{,2}^e|} \, \epsilon_{IKM} \left(\sum_{b=1}^{n} \left[(\boldsymbol{\eta}_{,2}^e)_M \hat{N}_{b,1} - (\boldsymbol{\eta}_{,1}^e)_M \hat{N}_{b,2} \right] \delta X_{bK}^e \right) d\hat{\Gamma} \tag{B.3}$$

whence it follows that

$$R_{bK}^{\text{int}} = \sum_{e=1}^{S} \int_{\hat{\Gamma}} \gamma \, \frac{(\boldsymbol{\eta}_{,1}^e \times \boldsymbol{\eta}_{,2}^e)_I}{|\boldsymbol{\eta}_{,1}^e \times \boldsymbol{\eta}_{,2}^e|} \, \epsilon_{IKM} \left[(\boldsymbol{\eta}_{,2}^e)_M \hat{N}_{b,1} - (\boldsymbol{\eta}_{,1}^e)_M \hat{N}_{b,2} \right] d\hat{\Gamma} \tag{B.4}$$

Likewise, taking variations of the volume constraint we obtain

$$\delta I_h^{\text{vol}} = -\alpha \left(V_2 - \int_{B_2} dV \right) \sum_{e=1}^{E_2} \int_{\Omega^e} \left(\sum_{b=1}^{n} \delta X_{bK}^e N_{b,K}^e \right) dV \tag{B.5}$$

where E_2 is the number of elements in B_2. From this identity we obtain

$$R_{bK}^{\text{vol}} = -\alpha \left(V_2 - \int_{B_2} dV \right) \sum_{e=1}^{E_2} \int_{\Omega^e} N_{b,K}^e \, dV \tag{B.6}$$

References

N. Amenta and M. Bern. Surface reconstruction by voronoi filtering. *Discrete & Computational Geometry*, 22(4): 481–504, 1999.

N. Amenta, S. Choi, T.K. Dey, and N. Leekha. A simple algorithm for homeomorphic surface reconstruction. *International Journal of Computational Geometry & Applications*, 12(1-2):125–141, 2002.

M.P. Bendsoe and N. Kikuchi. Generating optimal topologies in structural design using a homogenization method. *Computer Methods in Applied Mechanics and Engineering*, 71(2):197–224, 1988.

J.D. Eshelby. The elastic energy-momentum tensor. *Journal of Elasticity*, 5(3-4):321–335, 1975.

L.C. Evans. *Partial Differential Equations*. American Mathematical Society, Providence, Rhode Island, 1998.

L Freitag and C. Ollivier-Gooch. A comparison of tetrahedral mesh improvement techniques. In *Proceedings of the 5th International Meshing Roundtable*, pages 87–100, Pittsburgh, Pennsylvania, October 1996. Sandia National Laboratories.

M.E. Gurtin. The nature of configurational forces. *Archive for Rational Mechanics and Analysis*, 131:67–100, 1995.

M.E. Gurtin. *Configurational Forces as Basic Concepts of Continuum Physics*. Springer-Verlag Inc., New York, 2000.

C. M. Hoffmann. *Geometric and Solid Modeling*. Morgan Kaufmann Publishers, San Mateo, California, 1989.

T.Y. Hou, J.S. Lowengrub, and M.J. Shelley. Boundary integral methods for multicomponent fluids and multiphase materials. *Journal of Computational Physics*, 169(2):302–362, 2001.

B. Joe. Three-dimensional triangulations from local transformations. *SIAM Journal on Scientific and Statistical Computing*, 10:718–741, 1989.

B. Joe. Construction of three-dimensional improved-quality triangulations using local transformations. *SIAM Journal on Scientific Computing*, 16(6):1292–1307, November 1995.

C.S. Jog, R. Sankarasubramanian, and T.A. Abinandanan. Symmetry-breaking transitions in equilibrium shapes of coherent precipitates. *Journal of the mechanics and Physics of Solids*, 48(11):2363–2389, 2000.

W.C. Johnson and J.W. Cahn. Elastically induced shape bifurcations of inclusions. *Acta Metallurgica*, 32((11)), 1984.

H.J. Jou, P.H. Leo, and J.S. Lowengrub. Microstructural evolution in inhomogeneous elastic media. *Journal of Computational Physics*, 131(1):109–148, 1997.

M.F. Kanninen and C.H. Popelar. *Advanced Fracture Mechanics*. Oxford University Press, 1985.

P.H. Leo, J.S. Lowengrub, and H.J. Jou. A diffuse interface model for microstructural evolution in elastically stressed solids. *Acta Materialia*, 46(6):2113–2130, 1998.

P.H. Leo, J.S. Lowengrub, and Q. Nie. Microstructural evolution in orthotropic elastic media. *Journal of Computational Physics*, 157(1):44–88, 2000.

P.H. Leo, J.S. Lowengrub, and Q. Nie. On an elastically induced splitting instability. *Acta Materialia*, 49(14):2761–2772, 2001.

F. Z. Li, C. F. Shih, and A. Needleman. A Comparison of Methods for Calculating Energy Release Rates. *Engineering Fracture Mechanics*, 21:405–421, 1985.

M. Mantyla. *An Introduction to Solid Modeling*. Computer Science Press, Rockwille, Maryland, 1988.

K. Maute and E. Ramm. Adaptive topology optimization. *Structural Optimization*, 10(2):100–112, 1995.

K. Maute and E. Ramm. Adaptive topology optimization of shell structures. *AIAA Journal*, 35(11):1767–1773, 1997.

K. Maute, S. Schwarz, and E. Ramm. Structural optimization - the interaction between form and mechanics. *Zeitschrift für Angewandte Mathematik und Mechanik*, 79(10):651–673, 1999.

J.F. Molinari and M. Ortiz. Three-dimensional adaptive meshing by subdivision and edge-collapse in finite-deformation dynamic- plasticity problems with application to adiabatic shear banding. *International Journal for Numerical Methods in Engineering*, 53(5):1101–1126, 2002.

B. Moran and C. F. Shih. A general treatment of crack tip contour integrals. *International Journal of Fracture*, 35: 295–310, 1987.

M. Ortiz and L. Stainier. The variational formulation of viscoplastic constitutive updates. *Computer Methods in Applied Mechanics and Engineering*, 171(3-4):419–444, 1999.

D. M. Parks. A Stiffness Derivative Finite Element Technique for Determination of Crack-Tip Stress Intensity Factors. *International Journal of Fracture*, 10:487–502, 1974.

R. Radovitzky and M. Ortiz. Error estimation and adaptive meshing in strongly nonlinear dynamic problems. *Computer Methods in Applied Mechanics and Engineering*, 172(1-4):203–240, 1999.

R. Radovitzky and M. Ortiz. Tetrahedral mesh generation based on node insertion in crystal lattice arrangements and advancing-front-Delaunay triangulation. *Computer Methods in Applied Mechanics and Engineering*, 187:543–569, 2000.

A. A. G. Requicha. Representations for rigid solids: Theory, methods and systems. *Computing Surveys*, 12:437–465, 1980.

J.R. Rice. A path independent integral and the approximate analysis of strain concentration by notches and cracks. *Journal of Applied Mechanics*, 35:379–386, 1968.

P. Sampl. Medial axis construction in three dimensions and its application to mesh generation. *Engineering with Computers*, 17(3):234–248, 2001.

A. Schleupen, K. Maute, and E. Ramm. Adaptive fe-procedures in shape optimization. *Structural and Multidisciplinary Optimization*, 19(4):282–302, 2000.

I. Schmidt and D. Gross. The equilibrium shape of an elastically inhomogeneous inclusion. *Journal of the Mechanics and Physics of Solids*, 45:1521–1549, 1997.

S. Schwarz, K. Maute, and E. Ramm. Topology and shape optimization for elastoplastic structural response. *Computer Methods in Applied Mechanics and Engineering*, 190(15-17):2135–2155, 2001.

J. R. S. Shewchuk. An introduction to the conjugate gradient method without agonizing pain. Technical report, University of California, Berkeley, http://www.cs.berkeley.edu/ jrs, 1994.

Moran B. Shih, C. F. and T. Nakamura. Energy release rate along a three dimensional crack front in a thermally stressed body. *International Journal of Fracture*, 30:79–102, 1986.

G. Strang and G. J. Fix. *An Analysis of the Finite Element Method*. Prentice-Hall, Englewood Cliffs, N.J., 1973.

T. Sussman and K.J. Bathe. The gradient of the finite element variational indicator with respect to nodal point coordinates: An explicit calculation and applications in fracture mechanics and mesh optimization. *International Journal for Numerical Methods in Engineering*, 21:763–774, 1985.

Su C.S. Thomson, M.E. and P.W. Voorhees. The equilibrium shape of a misfitting precipitate. *Acta Metallurgica et Materialia*, 42:2107–2122, 1994.

P.W. Voorhees. The theory of ostwald ripening. *Journal of Statistical Physics*, 38(1-2):231–252, 1985.

P.W. Voorhees. Ostwald ripening of 2-phase mixtures. *Annual Review of Materials Science*, 22:197–215, 1992.

P.W. Voorhees, G.B. McFadden, R.F. Boisvert, and D.I. Meiron. Numerical-simulation of morphological development during ostwald ripening. *Acta Metallurgica*, 36(1):207–222, 1988.

P.W. Voorhees, G.B. McFadden, and W.C. Johnson. On the morphological development of 2nd-phase particles in elastically-stressed solids. *Acta Metallurgica et Materialia*, 40(11):2979–2992, 1992.